Available online at www.sciencedirect.com
ScienceDirect
Journal of Power Sources 180 (2008) 132–142
JOURNAL OF POWER SOURCES
www.elsevier.com/locate/jpowsour

Plasma sprayed metal supported YSZ/Ni–LSGM–LSCF ITSOFC with nanostructured anode

Changsing Hwang *, Chun-Huang Tsai, Chih-Hung Lo, Cha-Hong Sun

Physics Division, Institute of Nuclear Energy Research, Lungtan, Taoyuan 32546, Taiwan, ROC

Received 11 January 2008; accepted 22 January 2008
Available online 12 February 2008

Abstract

Intermediate temperature solid oxide fuel cells (ITSOFCs) supported by a porous Ni-substrate and based on Sr and Mg doped lanthanum gallate (LSGM) electrolyte, lanthanum strontium cobalt ferrite (LSCF) cathode and nanostructured yttria stabilized zirconia–nickel (YSZ/Ni) cermet anode have been fabricated successfully by atmospheric plasma spraying (APS). From ac impedance analysis, the sprayed YSZ/Ni cermet anode with a novel nanostructure and advantageous triple phase boundaries after hydrogen reduction has a low resistance. It shows a good electrocatalytic activity for hydrogen oxidation reactions. The sprayed LSGM electrolyte with ~60 μm in thickness and ~0.054 S cm^{-1} conductivity at 800 °C shows a good gas tightness and gives an open circuit voltage (OCV) larger than 1 V. The sprayed LSCF cathode with ~30 μm in thickness and ~30% porosity has a minimum resistance after being heated at 1000 °C for 2 h. This cathode keeps right phase structure and good porous network microstructure for conducting electrons and negative oxygen ions. The APS sprayed cell after being heated at 1000 °C for 2 h has a minimum inherent resistance and achieves output power densities of ~440 mW cm^{-2} at 800 °C, ~275 mW cm^{-2} at 750 °C and ~170 mW cm^{-2} at 700 °C. Results from SEM, XRD, ac impedance analysis and *I–V–P* measurements are presented here.

Keywords: Thermal plasma spraying; Nanostructured anode; Solid oxide fuel cells

1. Introduction

The solid oxide fuel cell (SOFC) is an electrochemical reactor that can directly transform the chemical energy of gaseous fuels such as hydrogen and natural gas into electrical power. Typical SOFC systems employ yttria stabilized zirconia (YSZ) as an electrolyte, yttria stabilized zirconia–nickel cermet (YSZ/Ni) as an anode and perovskite conducting oxides such as lanthanum manganites ($LaMnO_3$) as a cathode [1–3]. However, the high operating temperatures (900–1000 °C) required by the oxygen-ion conducting solid electrolyte to ensure sufficient ionic conduction (of up to 0.1 S cm^{-1}) prevent the wide diffusion of this energy producing system in spite of its high efficiency and low pollution. Reducing the operating temperature down to 600–800 °C provides both substantially technical and economical advantages, dramatical cost reduction of SOFC technology is expected since much less expensive materials can be applied to the stack and system integration [4]. Furthermore, as the operating temperature is reduced, the system reliability and its operational life increase so that the possibility of using SOFCs for a wide range of applications, including both residential and automotive applications, increases.

However, as the operating temperature decreases to 600–800 °C, the energy loss of SOFC increases, due to significant increases in the bulk resistance of electrolyte and in the resistances of electrodes [5]. To reduce the energy loss from electrolyte, one way is to use thinner YSZ electrolytes (~5 μm) [5]; the other way is to use a higher conductivity electrolyte such as Sr and Mg doped lanthanum gallate (LSGM) [6–8]. To reduce the energy losses from electrodes, one way is to use highly active mixed ionic-electronic electrode materials, such as lanthanum strontium cobaltite (LSCo) or lanthanum strontium cobalt ferrite (LSCF) for cathode [9–11]; the other way is to use nanostructured composite electrodes [12]. Both nanostructured composite electrodes and highly active mixed ionic-electronic electrode materials are expected to provide more triple-phase boundaries (TPB) that extend well into electrodes so that

* Corresponding author. Tel.: +886 3 4711400x7311; fax: +886 3 4711408.
E-mail addresses: cshwang@iner.gov.tw, chansin.hwang@msa.hinet.net (C. Hwang).

0378-7753/$ – see front matter © 2008 Elsevier B.V. All rights reserved.
doi:10.1016/j.jpowsour.2008.01.075

catalytically assisted electrochemical reactions in electrodes can be enhanced.

Several approaches of fabricating SOFC cell elements exist. They include chemical vapor deposition (CVD), electrochemical vapor deposition (EVD), sol–gel method, tape-casting, screen-printing, physical vapor deposition (PVD) and thermal plasma spraying [13–23]. Among these approaches, atmospheric plasma spraying (APS) is a fast process, no or only slight postprocessing of the product is necessary. It is also known that the conventional wet coating processes, such as tape-casting and screen-printing, have to pass through several high temperature sintering processes for fabricating solid oxide fuel cells. These processes can easily introduce defects such as warps and crackles. Sometimes the requirement for having dense electrolyte, electrode porosity and good electrochemical layer contact can make these high temperature sintering processes very complex and contradictory. High temperature sintering processes can also induce reactions between function layers, such as reaction between LSGM electrolyte and Ni in the anode, so that an insulation phase such as lanthanum–nickel oxide is produced and cell internal resistance increases, but APS process is a fast sintering process, interaction between LSGM and Ni can be reduced [24,25]. In addition to high material deposition rates, APS processes can easily control the component composition and microstructure through variation of spray parameters, hence, plasma spraying process has thus appeared as a promising candidate for inexpensive and fast cell production, and attracted much attention [25–27].

Dense LSGM electrolytes have been successfully deposited by atmospheric plasma spraying on tubular and planar porous LSM substrates [28,29], after finishing LSGM coatings, porous anodes such as YSZ/Ni or SYT (yttrium doped strontium titanate) are also deposited by atmospheric plasma spraying to form cathode supported solid oxide fuel cells [29–31]. But in this paper, nanostructured YSZ/NiO anode, LSGM electrolyte and LSCF cathode are deposited on porous Ni substrates by atmospheric plasma spraying in sequence to make a metal supported solid oxide fuel cell. The advantage of a metal supported SOFC is to improve the mechanical strength of fuel cell so that a larger cell area of SOFC fabricated by APS processes is effective in cost and can be applied in the harsh environment. Applying nanostructured YSZ/Ni as anode, mixed ionic-electronic LSCF as cathode and high ion conductivity LSGM as electrolyte, a 600–800 °C intermediate temperature SOFC (ITSOFC) with a high power density is expected to be obtained.

2. Experiments

The APS consists of mainly a Praxair SG-100 dc plasma torch with Mach I nozzle that inject a high temperature plasma flame under atmospheric condition, two powder feeder systems for delivering plasma sprayable powders, a cooling system for the torch, a furnace for preheating the substrate, an IR detector for measuring the temperature of the substrate, a Fanuc Robot ARC Mate 120iB system to scan plasma torch and a fast CCD camera to observe trajectories of particles in the plasma flame. Fig. 1 schematically depicts the experimental set-up. The Praxair SG-100 dc plasma torch with Mach I nozzle is operated at currents up to 550 A. The gas mixed from argon and hydrogen, or mixed from argon and helium, or mixed from argon, hydrogen and helium is used as plasma forming gas. These mixed gases are simply delivered from a homemade mixing device that consists of mainly a Y shape mixing tube, a flexible spiral tube and three Brooker's mass flow controllers. Argon flow rates up to 60 slpm, hydrogen flow rates up to 15 slpm and helium flow rates up to 30 slpm are controlled by using these Brooker's mass flow controllers respectively. The plasma forming gas is injected uniformly into the gap between the anode and the cathode through gas injector to generate vortex gas flows between the anode and the cathode. A shroud gas can be provided to reduce the mixing of the surrounding air into the plasma flame. A cooling water is driven at ~50 l min^{-1} flow rate from the anode to the cathode using a ~10 kg cm^{-2} high pressure pump to cool the copper anode and the thoriated tungsten cathode.

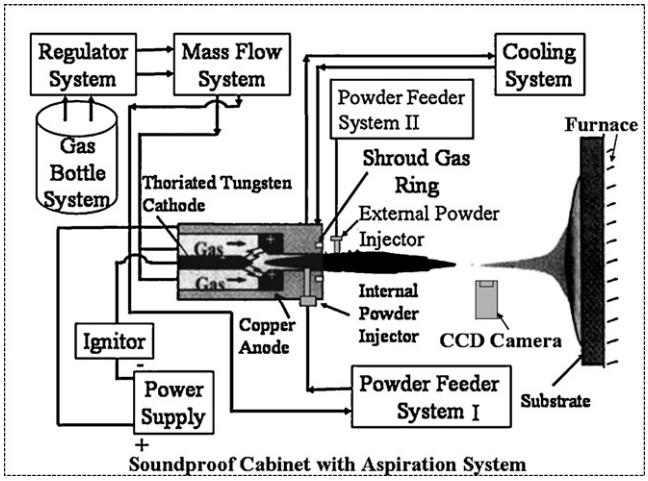

Fig. 1. Schematic drawing of APS plasma spray system.

Commercially available agglomerated powders of YSZ/NiO and LSCF ($La_{0.58}Sr_{0.4}Co_{0.2}Fe_{0.8}O_3$)/C purchased from Inframat Inc., USA and sintered powders of LSGM ($La_{0.8}Sr_{0.2}Ga_{0.8}Mg_{0.2}O_3$) purchased from Specialty Ceramics of Praxair, USA were applied in this study. YSZ/NiO powders have an average agglomerate size of 30–40 μm and an agglomerated composition of 8 mol% yttria-stabilized zirconia nanopowders (99.9%, particle size: 40–60 nm, 50 vol% after reduction), black NiO nanopowders (99.9%, particle size: 20–50 nm, 50 vol% after reduction) and a polyvinyl alcohol (PVA) organic binder. LSCF/C powders in spherical granule morphology and containing 15 wt% carbon black as a pore former have average granule sizes from 30 to 40 μm and submicron LSCF particle sizes that are less than 400 nm. LSGM powders made by spray granulation and sintering have a d50 particle size about 37 μm and an average surface area about 0.52 m^2 g^{-1}. These powders kept in approximately spherical granule morphology are flowable for plasma spray applications. SEM photos of these YSZ/NiO, LSGM and LSCF/C powders are shown in Fig. 2a–c. YSZ/NiO and LSGM powders are injected internally into the high temperature plasma flame as shown in Fig. 1. To produce a good bonding and porous

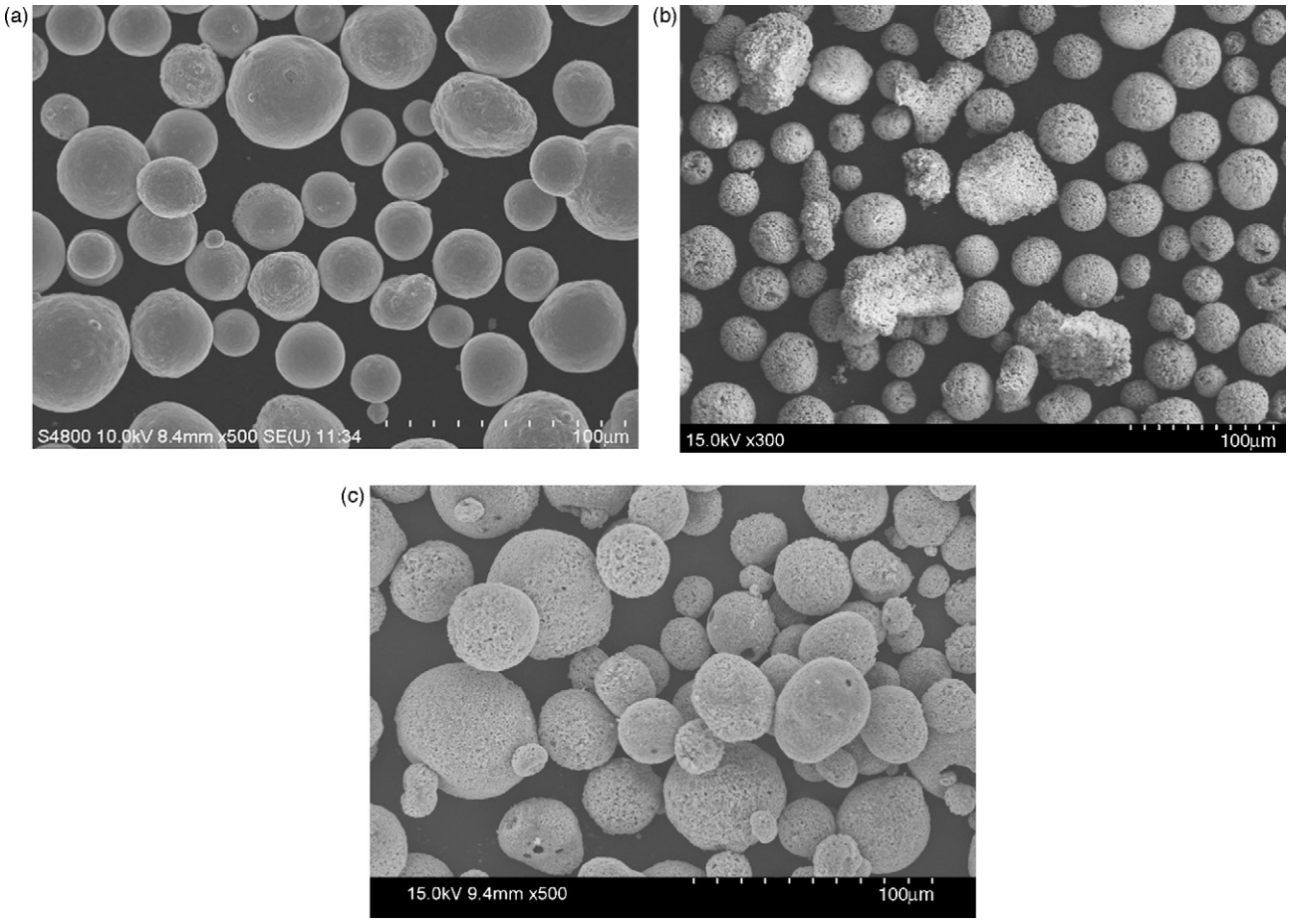

Fig. 2. SEM photos of powders: (a) YSZ/NiO, (b) LSGM and (c) LSCF/C used to fabricate ITSOFCs.

functional anode layer, YSZ/NiO powders are injected at a position away from the arc region inside the torch, but for having a gastight electrolyte layer, LSGM powders are injected at a position closer to the arc region inside the torch so that most LSGM powders can be fully melted. To produce a highly porous cathode and avoid decomposing the LSCF material, LSCF/C powders are injected externally into the high temperature plasma flame.

When YSZ/NiO and LSCF/C agglomerated powders enter the plasma flame generated by dc plasma torch, the PVA binder burns off, and part of residual ceramic powders is then heated and accelerated by the plasma flame to form YSZ/NiO and LSCF coatings. To make button cells for performance measurements, Φ24 mm porous nickel plates purchased from Applied Porous Technologies, USA with 1.2 mm in thickness and ∼25% porosity are used as substrates for coating. Original porous nickel substrates have pores larger than 100 μm. These pores are difficult to be covered by APS thin coatings and will induce pinholes on the electrolyte layer produced by APS coating process [32,33]. The surface of porous nickel substrate has to be modified to reduce the pore sizes to around 10 μm. A furnace with controllable temperatures is applied to preheat porous nickel substrates. Before plasma-spraying, the substrate is preheated to a preset temperature (300–500 °C). After spraying YSZ/NiO powders onto a preheated porous nickel substrate, LSGM powders are then sprayed onto the YSZ/NiO layer to form an electrolyte layer, and then LSCF/C powders are sprayed onto the LSGM electrolyte layer to form a cathode. During plasma spraying, SG-100 torch is scanned by a robot arm (Fanuc Robot ARC Mate 120iB system). The speed of robot arm can be adjusted to be as high as 1000 mm/s. An aspiration system is adopted to suck materials generated during the evaporation of PVA binder. All coating experiments are conducted in the soundproof cabinet shown in Fig. 1 to reduce the sound noise generated by the plasma torch. After producing a button cell, the whole cell is heated up to ∼1000 °C for 2 h to reduce stresses produced by plasma spray and to increase powder bonding strengths in each layer and between layers. Table 1 presents typical operating parameters. The performance of whole button cell with Pt pastes on both sides of cell is measured by the system that combines a ProboStat (NorECs AS, Norway) with Solartron 1255 and Solartron 1287 (Solartron Analytical, UK). Both electric power density and ac impedance of button cell are measured. A 10 mV ac signal with frequencies varied from 0.1 to 1 MHz is applied in the ac impedance measurement. The scheme for measuring output power densities and ac impedances of APS plasma sprayed cells is shown in Fig. 3. To calibrate the resistance R_{lead} and inductance L_{lead} contributed from Pt lead wires, connections and contacts inside the ProboStat, the ac impedance result obtained by removing tested cell and allowing direct contact between Pt

Table 1
Typical experimental parameter values of atmospheric plasma spraying.

Spray parameter	Anode	Electrolyte	Cathode	Unit
Torch power	28–30	30–32	27–29	kW
Torch current	~450	~500	~430	A
Primary argon flow rate	48–58	48–58	48–58	slpm
Secondary helium flow rate	16–26	16–26	16–26	slpm
Secondary hydrogen flow rate	4–9	4–9	4–9	slpm
Powder feed rate	2–10	2–10	2–10	g min^{-1}
Argon carry gas flow rate	2–5	2–5	2–5	slpm
Spray distance	9–11	9–11	9–11	mm
Preheated substrate temperature	300–500 °C	300–500 °C	300–500 °C	°C
Shroud gas flow rate	0	40–60	0	slpm
Robot scan speed	300–500	300–500	300–500	mm s^{-1}

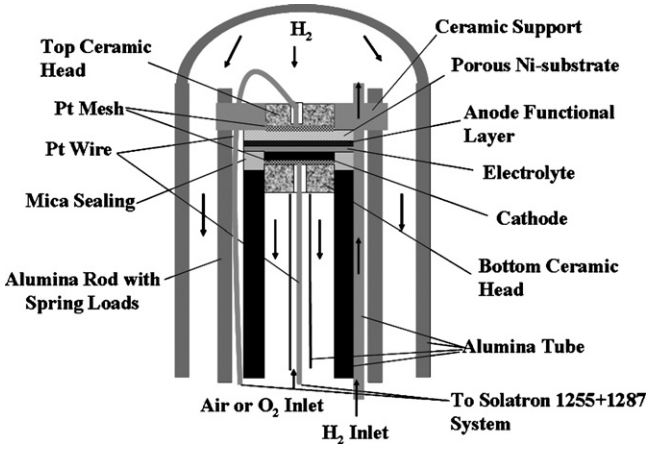

Fig. 3. The scheme of testing APS sprayed cells.

meshes of cathode and anode sides shown in Fig. 3 was measured and analyzed by the circuit model shown in Fig. 4. The obtained R_{lead} and L_{lead} are 0.378 Ω cm^2 and 4.45×10^{-7} H cm^{-1}. SEM, XRD and EDX apparatuses are adopted to analyze the coatings prepared in this work.

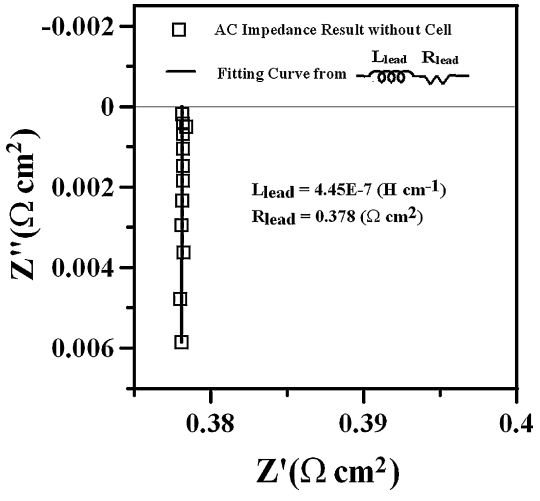

Fig. 4. ac impedance data measured without tested cell in the ProboStat and fitting curve from R_{lead} and L_{lead} in series, $R_{lead} = 0.378\ \Omega\ cm^{-2}$ and $L_{lead} = 4.45 \times 10^{-7}$ H cm^{-1}.

3. Results and discussions

3.1. Characterization of nanostructured YSZ/Ni cermet anode functional layer

In order to minimize anode resistance, the porous YSZ/NiO coating is deposited by injecting YSZ/NiO powders containing nanoYSZ and NiO powders into the APS high temperature plasma flame. Fig. 5 shows a nanostructured surface morphology of plasma sprayable micron YSZ/NiO powder. It is an agglomerate of the original nanoYSZ and NiO powders. The surface morphology of YSZ/NiO film with a thickness about 20 μm is given in Fig. 6. The corresponding XRD pattern of this YSZ/NiO coating on porous nickel substrate is given in Fig. 7. The nickel peaks come from the porous nickel substrate. The YSZ/Ni anode functional layer is converted from YSZ/NiO coating through the hydrogen reduction process at cell operating condition. The observed nanostructured surface morphology of this YSZ/Ni anode functional layer is given in Fig. 8. NiO particles in the YSZ/NiO coating are reduced into Ni particles. YSZ particles are distinguished from Ni particles by comparing secondary electron imaging (SEI) and backscattered electron imaging (BEI) images at the same observed position. These SEI and BEI images are

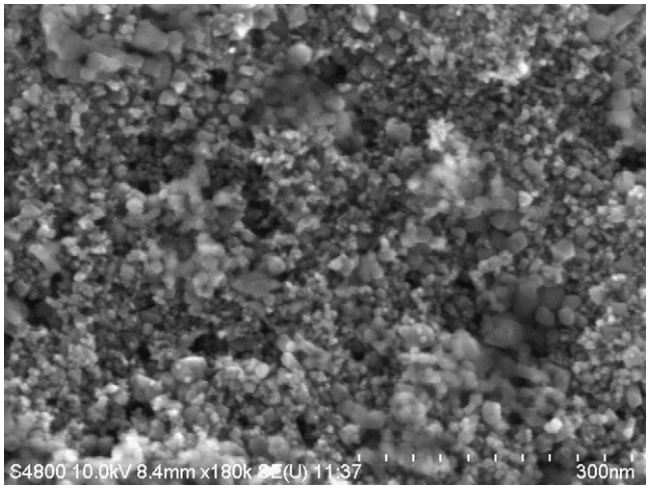

Fig. 5. Nanostructured surface of a plasma sprayable micron YSZ/NiO powder containing the original nanoYSZ and NiO powders.

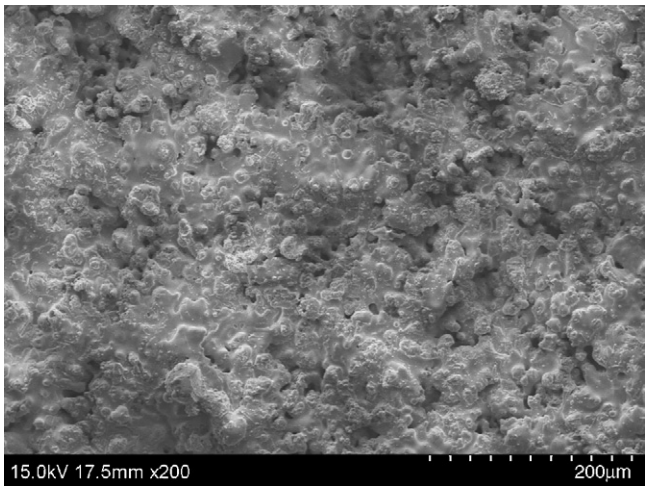

Fig. 6. Surface morphology of APS sprayed YSZ/NiO film.

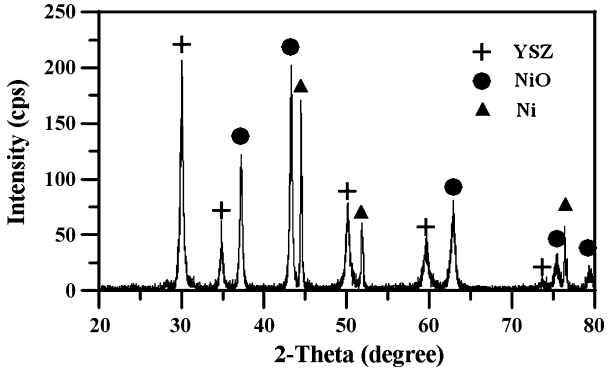

Fig. 7. XRD pattern of YSZ/NiO coating on a porous nickel substrate.

shown in Fig. 9a and b. Because the brightness of BEI element image is proportional to the electron density of element and the electron density of nickel element has a factor about 1.5 times larger than the electron density of zirconium element, the larger and brighter particles in Fig. 9b and the larger gray particles in Fig. 8 are nickel elements, they form a network for conducting electrons. The network structure formed by smaller particles shown in Figs. 8 and 9a contains zirconium element, they form a network for conducting negative oxygen ions. The nano-pores shown in Fig. 8 enables the flow of hydrogen gas.

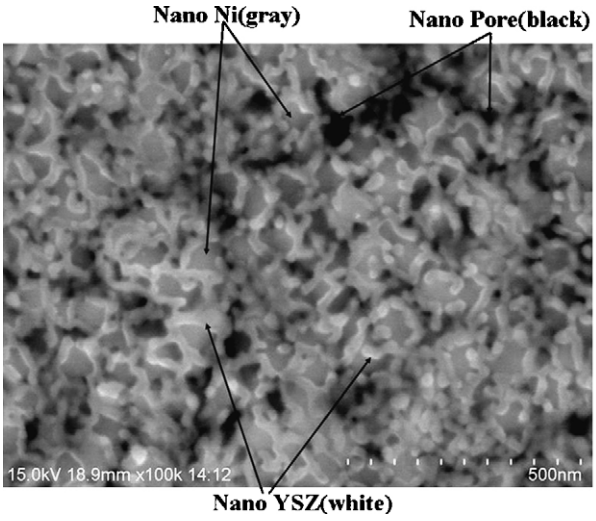

Fig. 8. Nanostructured surface morphology of a YSZ/Ni functional layer.

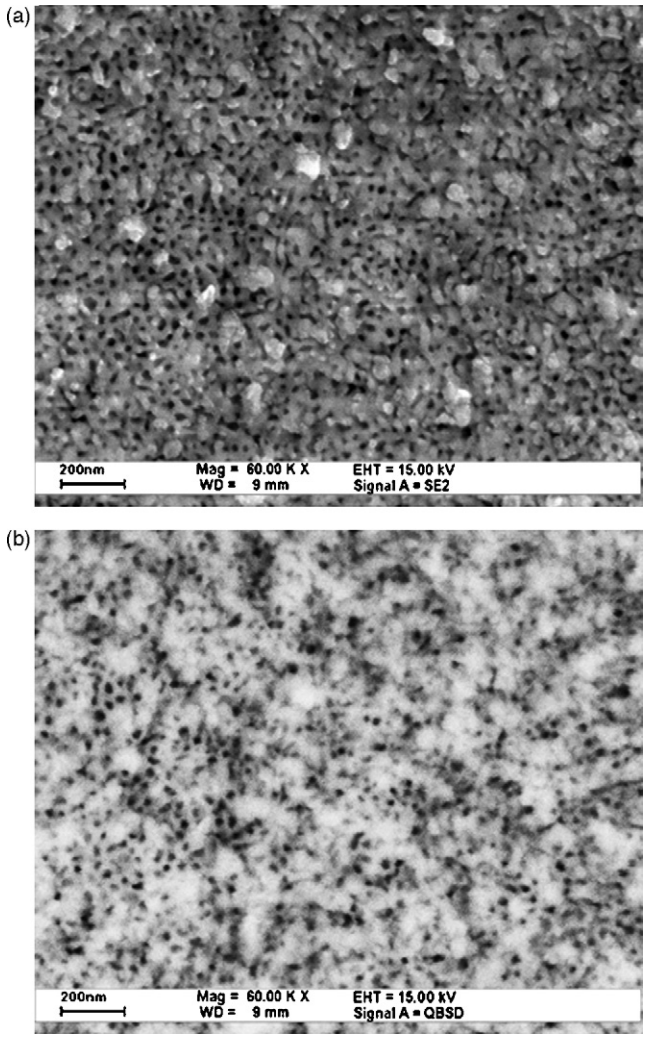

Fig. 9. (a) SEI and (b) BEI surface images of a nanostructured YSZ/Ni anode functional layer.

In Fig. 8, the nano-scaled Ni particles appear to be wrapped by the nanostructured YSZ network, and nickel and YSZ networks interlace. Hydrogen oxidation reactions are well known to occur on the triple phase boundaries (TPB) formed by pores, YSZ particles and nickel particles [25,26]. The nanostructured YSZ/Ni anode coating produced herein can provide significantly larger triple phase boundaries for hydrogen oxidation reactions than those in the microstructured YSZ/Ni coating [34,35].

3.2. Characterization of LSGM electrolyte layer

The X-ray diffraction patterns of LSGM feedstock powders and as-sprayed film on the top of YSZ/NiO layer are shown in Fig. 10. The LSGM powder is characterized by a single phase, nevertheless, the as-sprayed LSGM film has a small amount of amorphous phase identified by a broaden peak at a 2θ angle less than 32°. In order to find the temperature to re-crystallize the

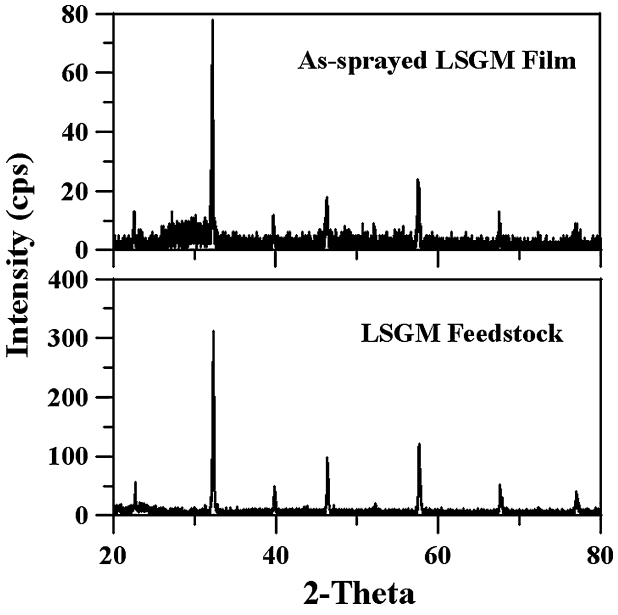

Fig. 10. X-ray diffraction patterns for LSGM feedstock powder and as-sprayed film.

amorphous phase of as-sprayed LSGM film, four LSGM films were heated at 600, 700, 800 and 900 °C for 1 h, respectively. The XRD data shown in Fig. 11 indicates that LSGM films become a high degree of crystallization and have the same XRD

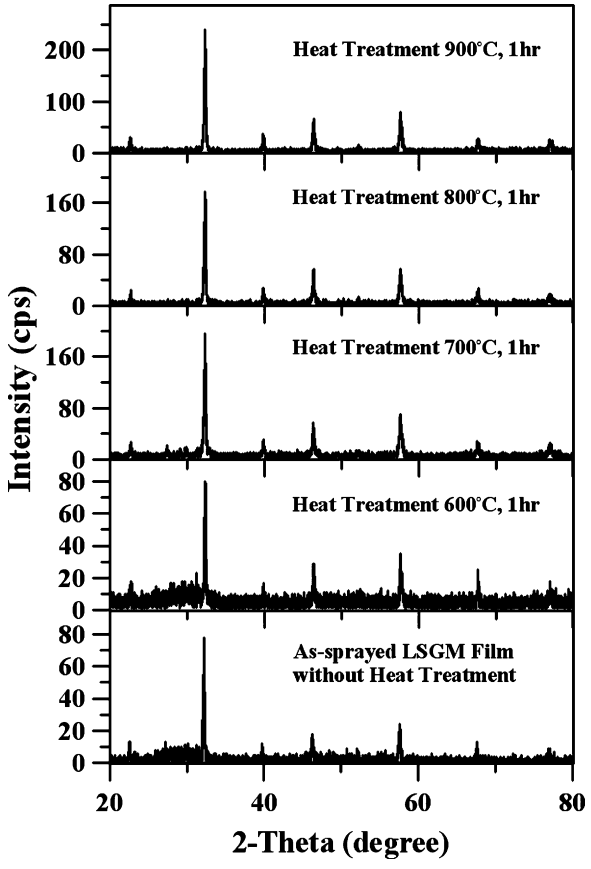

Fig. 11. X-ray diffraction patterns of APS sprayed LSGM film with and without heat treatment.

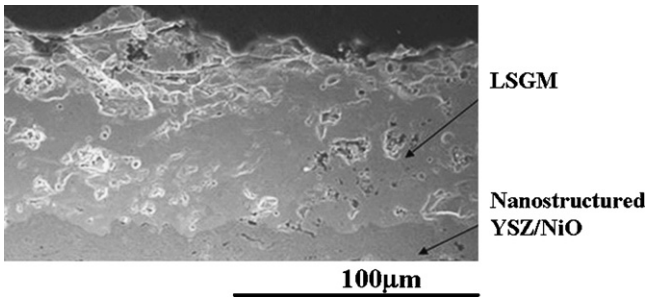

Fig. 12. SEM cross-sectional view of APS sprayed LSGM film.

peaks as powders after being heated at temperatures higher than 700 °C for 1 h. This indicates that the crystal structure of LSGM film can be completely recovered by an intermediate temperature heat treatment and the chemical stoichiometry of LSGM film is not altered by the APS coating process. Fig. 12 shows a SEM cross-sectional image of as-sprayed LSGM film on the YSZ/NiO layer. A high density crack free LSGM layer with a thickness about 50–60 μm and a satisfactory interfacial contact to the nanostructured YSZ/NiO layer can be formed by atmospheric plasma spraying. There are closed pores formed in the LSGM film. An Arrhenius plot of LSGM film obtained from analyzing ac impedance data measured at the open circuit condition and different temperatures is given in Fig. 13 [6,36]. The estimated LSGM activation energy for conducting oxygen ions is ~0.72 eV (600–800 °C) that is slightly higher than ~0.63 eV (800 °C) reported by Ishihara et al. [37]. The measured conductivity of the LSGM layer is ~0.054 S cm^{-1} (800 °C) that is lower than 0.105 S cm^{-1} for sintered LSGM at 1400 °C reported by Lee et al. [6]. The lower conductivity of APS sprayed LSGM film could be explained by the existence of closed pores inside the film.

3.3. Characterization of LSCF cathode layer

In order to decrease the interfacial polarization at the interface between electrolyte and cathode, triple phase boundaries

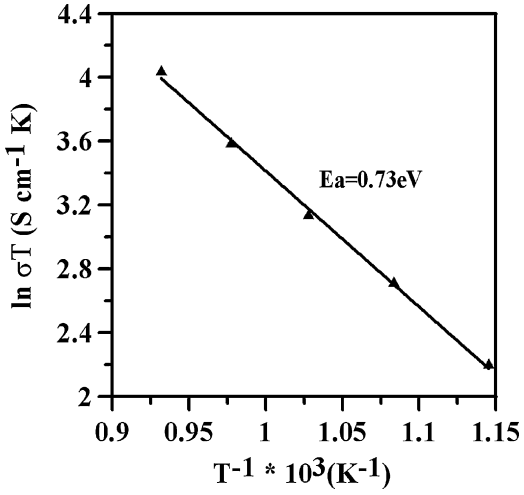

Fig. 13. Arrhenius plot of the APS sprayed LSGM film.

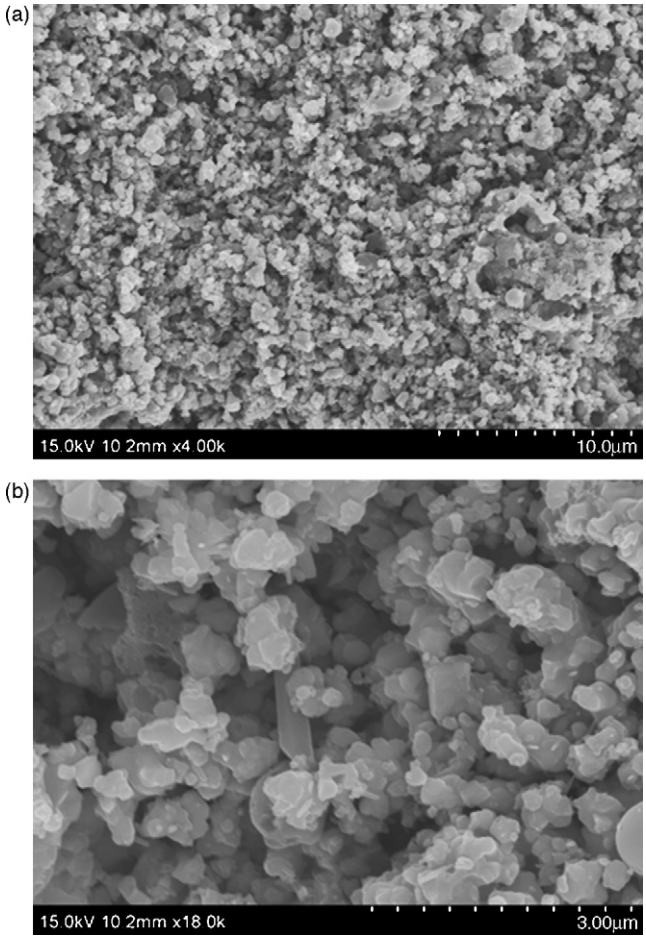

Fig. 14. Fractured cross-sections of as-sprayed LSCF cathode: (a) in low magnification and (b) in high magnification.

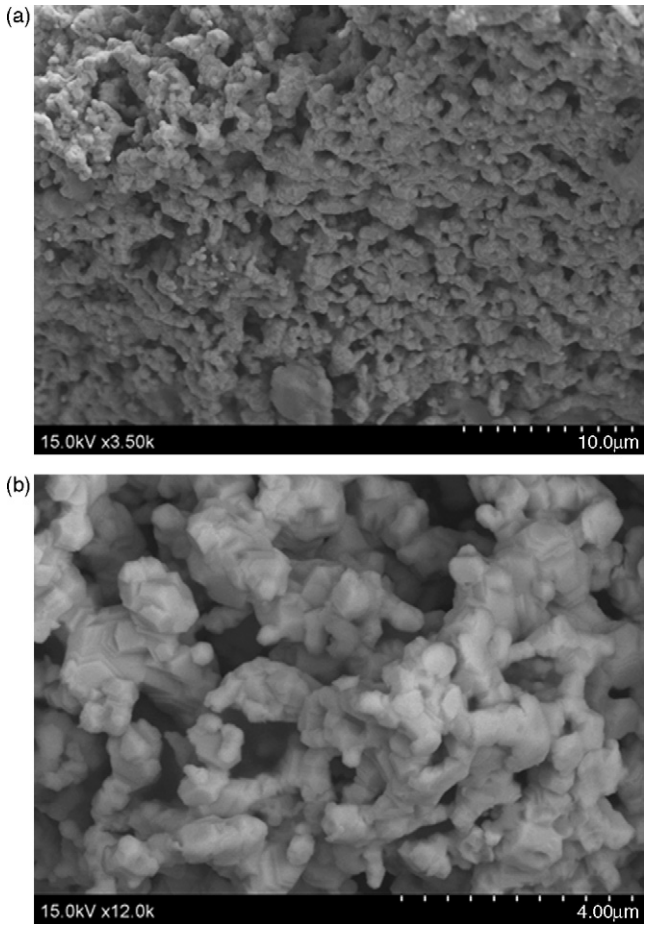

Fig. 15. Fractured cross-sections of the heated LSCF cathode at 1000 °C for 2 h: (a) in low magnification and (b) in high magnification.

at this interface for reduction reaction of oxygen gas must be increased. Because LSCF is a mixed ionic electronic conducting material, porous LSCF cathodes have these reaction sites extended from the interface into cathode body. Good adhesion of LSCF to LSGM electrolyte and right microstructure and thickness of porous LSCF cathode are important factors to minimize the cathode polarization resistance [7]. Fig. 14a and b shows fractured cross-sections of as-sprayed LSCF cathode in low and high magnifications. To remove carbon residue in the cathode coating, to optimize the cathode microstructure and improve the bonding between LSCF particles, the as-sprayed LSCF coating was heated at 1000 °C for 2 h. Fig. 15a and b gives the fractured cross-sections of this heated LSCF cathode coating. The difference of particle sizes between as-sprayed and heated LSCF cathodes is insignificant, but the 3D porous network microstructure of APS sprayed LSCF cathode is more obvious after this heat treatment. The estimated porosity of this LSCF cathode shown in Fig. 15b by image analysis is about ∼30%. Fig. 16 gives the XRD diffraction patterns of LSCF powders and the heated LSCF cathode coating. No apparent difference between these diffraction patterns indicates that the LSCF perovskite structure is preserved in the APS cathode coating processes. Fig. 17a and b shows the fractured and polished cross-sections of LSCF cathode deposited on LSGM electrolyte. This LSCF cathode and LSGM electrolyte have been heated at ∼1000 °C for 2 h. The deposited LSCF cathode has an average thickness of 20–30 μm. No delamination between cathode and electrolyte is observed. It is believed that the post-heat treated LSCF cathode deposited by APS process has a good adhesion to electrolyte, enough pores for oxygen gas diffusion, a proper network for conducting electrons

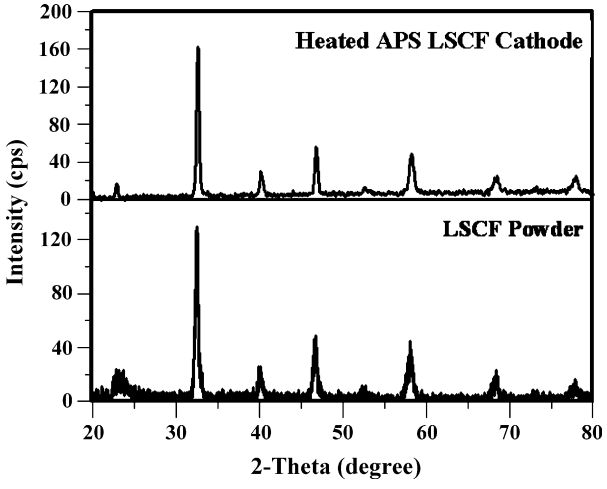

Fig. 16. XRD diffraction patterns of LSCF powders and the heated LSCF cathode at 1000 °C for 2 h.

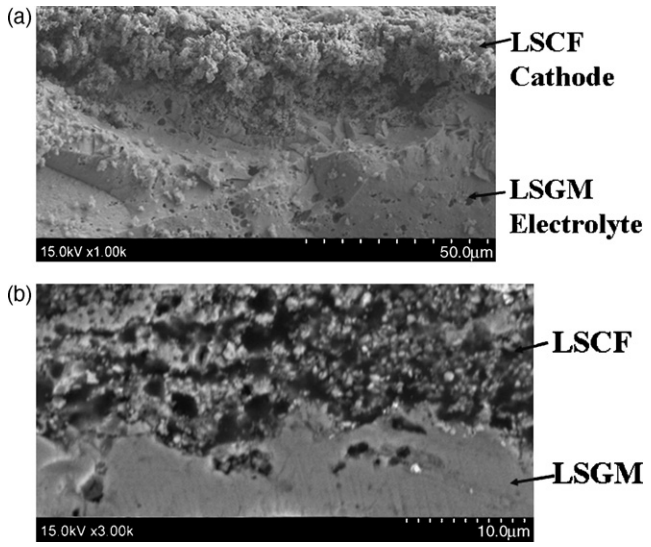

Fig. 17. Cross-sections of LSCF cathode and LSGM electrolyte after being heated at 1000 °C for 2 h: (a) fractured and (b) polished.

and negative oxygen ions and a sufficient thickness to approach a critical thickness of minimum polarization resistance [7].

3.4. Characterization of the YSZ/Ni–LSGM–LSCF cell

The polished cross-section of an APS plasma sprayed YSZ/Ni–LSGM–LSCF cell is shown in Fig. 18. This cell has been heated at 1000 °C for 2 h and tested to measure OCV values for ~55 h. The layer structure of LSCF, LSGM and YSZ/Ni coatings deposited by APS process on a porous nickel substrate is shown here. The good adhesion between coatings is observed. The thicknesses of LSCF, LSGM and YSZ/Ni coatings shown in Fig. 18 are 20–30, 50–60 and 10–20 μm, respectively. The corresponding open circuit voltage (OCV) curve of this cell is shown in Fig. 19. The OCV curve was measured when the button cell was heated at a rate of 1 °C min^{-1} from room temperature to 800 °C. The flow rates of oxygen gas for cathode and humidified hydrogen gas for anode are 100 cm^3 min^{-1} in the OCV measurement. The humidified hydrogen gas contains 3 vol% water vapor. The open circuit voltage larger than 1 V implies that the pores in LSGM electrolyte shown in Fig. 18 are closed pores. The *I* (current density)–*V* (voltage) and *I*–*P* (power) performance data of this APS sprayed cell in the temperature range of 700–800 °C with oxygen and humidified hydrogen as operating gases are given in Fig. 20. The gas flow rates of oxygen and humidified hydrogen are 300 cm^3 min^{-1}. It is observed that the maximum power density of ~440 mW cm^{-2} at 800 °C decreases to ~275 mW cm^{-2} at 750 °C and to 170 mW cm^{-2} at 700 °C. These maximum power densities occur approximately at a cell voltage about 0.5 V. To reduce stresses produced by APS plasma spray and increase the bonding strengths between powders in each layer and between layers, the sprayed YSZ/Ni–LSGM–LSCF cells were heated as a whole at 820, 950, 1000, 1050, 1100 and 1150 °C for 2 h, respectively. The corresponding Cole–Cole plots of ac impedance results measured at 800 °C for these sprayed cells are given in Fig. 21. The equivalent circuit model for analyzing these ac impedance data is also shown in this figure [38–40]. R_{lead} and L_{lead} must be included in this circuit model to consider contributions from Pt lead wires, connections and contacts inside the ProboStat. The continuous color curves are obtained from the

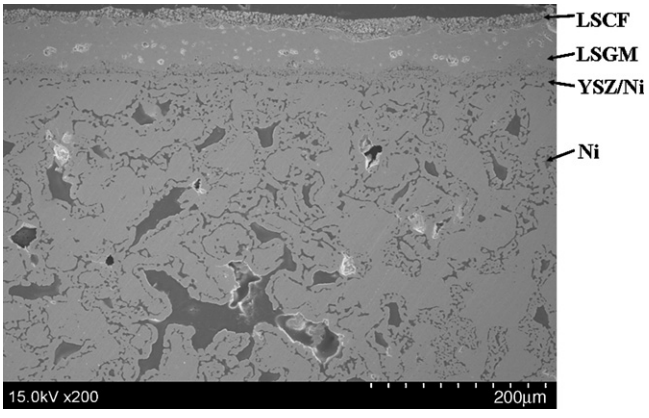

Fig. 18. Polished cross-section of APS sprayed YSZ/Ni–LSGM–LSCF cell having a heat treatment at 1000 °C for 2 h and a OCV test for ~55 h.

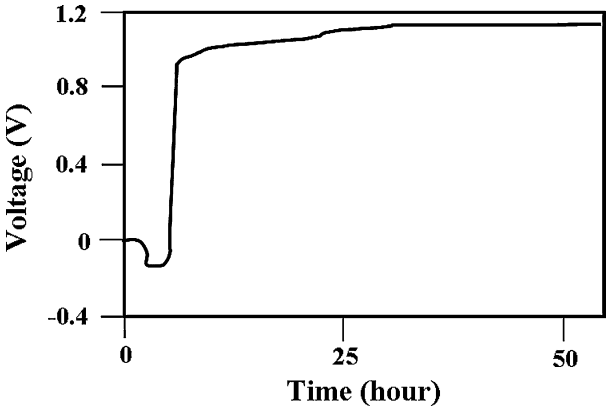

Fig. 19. Measured open circuit voltage history at 800 °C for the APS sprayed YSZ/Ni–LSGM–LSCF cell.

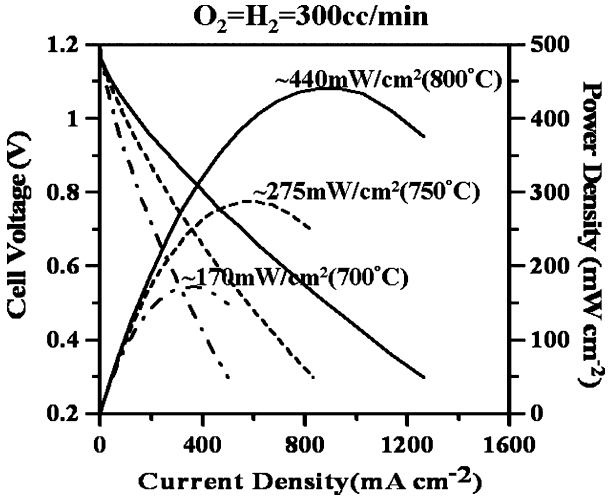

Fig. 20. Typical *I*–*V* and *I*–*P* curves obtained at 300 cm^3 min^{-1} gas flow rates of oxygen and humidified hydrogen for the sprayed cell having a heat treatment at 1000 °C for 2 h.

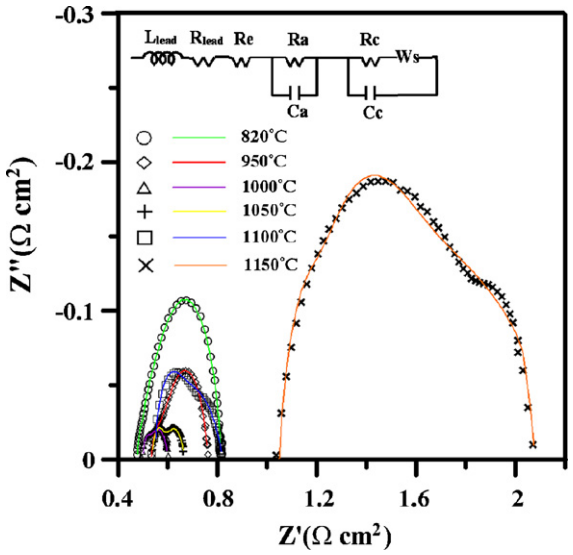

Fig. 21. Cole–Cole plots of ac impedance measurements at 800 °C for the sprayed cells heated at 820, 950, 1000, 1050, 1100 and 1150 °C, respectively for 2 h and the equivalent circuit model for fitting ac impedance results.

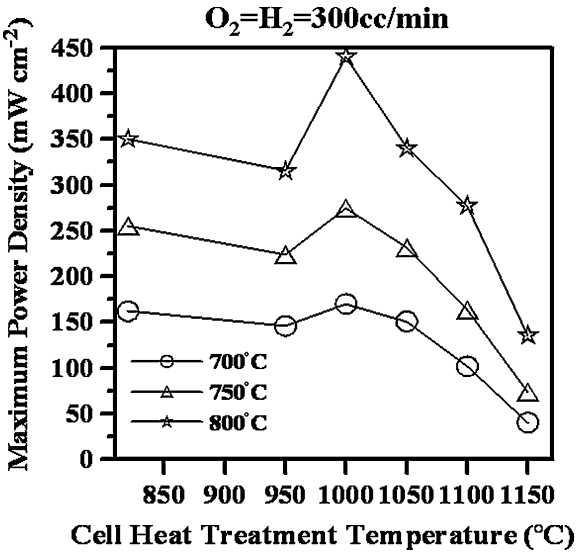

Fig. 23. Maximum power densities of cells vs. heat treatment temperatures.

fittings of this equivalent circuit model. In this equivalent circuit model, Re is used to simulate electrolyte resistance, Ra is used to simulate anode resistance, Rc is used to simulate cathode resistance, Ws is a generalized finite length Warburg element for a short-circuit terminus model [38,41] and is applied to simulate cathode diffusion and mass transport effect [38], Ca and Cc are applied to simulate interface capacitances across the anode–electrolyte and cathode–electrolyte interfaces [38,39]. The Warburg element Ws is a function of Ws − r (unit in Ω cm^2), Ws − t (unit in s) and Ws − p (dimensionless). This equivalent circuit model fits the experimental results very well with χ^2 less than 2×10^{-4}. The fitting parameter values of Re, Ra and Rc + Ws − r versus heat treatment temperature are given in Fig. 22. As discussed in the previous works [7,9], the total polarization resistance Rp is the difference between low and high frequency intercepts of ac impedance data on Z' real axis. Rp versus heat treatment temperature is also plotted in the same figure. In the equivalent circuit model, only resistors can consume energy. If the inherent resistance loss contributed by resistors in the equivalent circuit model of cell is minimized, then the cell driven by the electromotive force can deliver a highest output power density [39]. As shown in Fig. 22, Ra is significantly less than Re, Rc + Ws − r and Rp, hence the energy loss of anode is

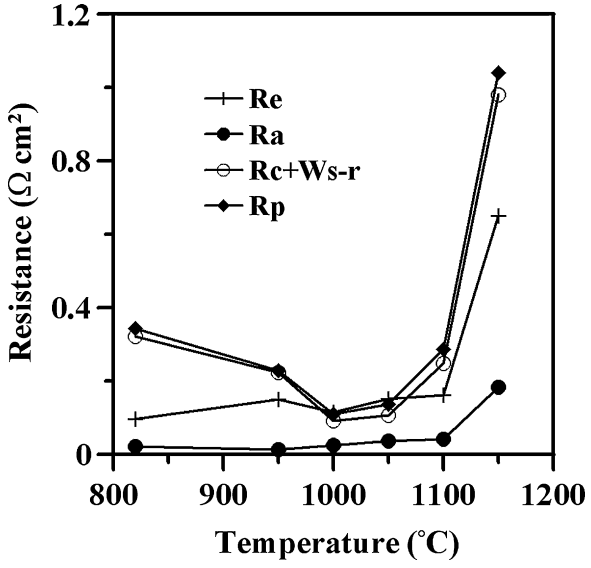

Fig. 22. Variations of Re, Ra, Rc + Ws − r and Rp vs. heat treatment temperatures.

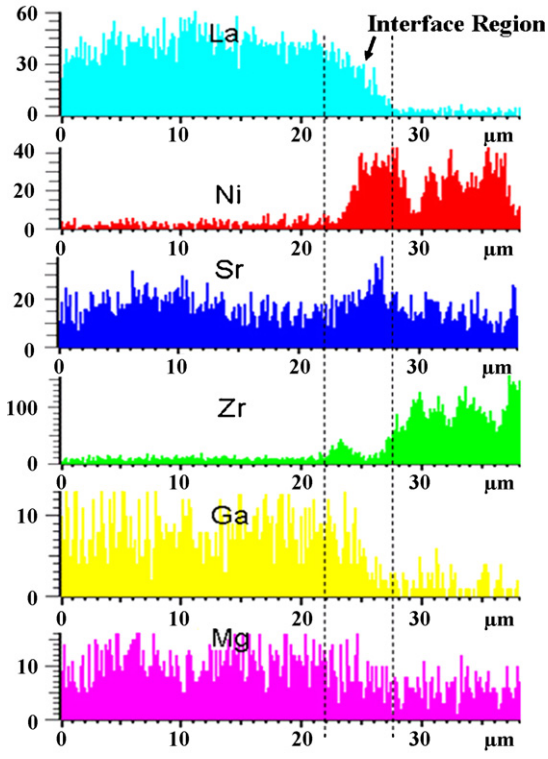

Fig. 24. EDX line scans of La, Ni, Sr, Zr, Ga and Mg elements across the anode–electrolyte interface of APS sprayed cell having a heat treatment at 1150 °C for 2 h.

smaller than that of cathode. The nanostructured YSZ/Ni cermet anode has a smaller resistance than LSCF cathode, and the major contribution in the total polarization resistance Rp comes from LSCF cathode. This figure also shows that the variations of Re and Ra in the heat treatment temperature range less than 1100 °C are small so that Re and Ra can be approached by constant values in this temperature range, this implies that the effects of variations of anode and electrolyte structures on cell performance are insignificant in this heat treatment temperature range. But, Rc + Ws − r and Rp have a large variation in the same temperature range, this implies that the effect of cathode structure's variation on cell performance in this heat treatment temperature range is significant. Because both Rc + Ws − r and Rp have a minimum at 1000 °C, hence, the cell after being heated at 1000 °C for 2 h is expected to deliver a maximum power density which is shown in Fig. 23. As the heat treatment temperature becomes larger than 1100 °C, Ra, Re, Rc + Ws − r and Rp shown in Fig. 22 start to increase steeply. The steep increases of Ra and Re can be explained by the interaction of LSGM electrolyte with YSZ/Ni anode to produce a high resistive material such as lanthanum–nickel oxide around the interface between LSGM electrolyte and YSZ/Ni anode [24,25]. Fig. 24 gives EDX line scans of La, Ni, Sr, Zr, Ga and Mg elements across the electrolyte–anode interface of a sprayed cell that was heated at 1150 °C for 2 h. It is found that the element inter-diffusion between anode and electrolyte occurs seriously at this heat treatment temperature. The size of this inter-diffusion layer is about 10 μm. For heat treatment temperatures higher than 1100 °C, the element inter-diffusion is the main cause to produce a high resistive material such as lanthanum–nickel oxide. The steep increases of Rc + Ws − r and Rp can be explained by the change of cathode microstructure as shown in Fig. 25a and b. The sprayed cell that was heated at 1000 °C for 2 h has a relatively uniform and fine porous cathode microstructure, but the sprayed cell that was heated at 1150 °C for 2 h has many dense areas in the cathode. It is believed that the cathode having been heated at 1150 °C for 2 h has less triple phase boundaries than the cathode that has been heated at 1000 °C for 2 h. The dense areas in the cathode are also unfavorable for oxygen gas propagation. Therefore, a proper heat treatment is needed for getting a right microstructure of LSCF cathode.

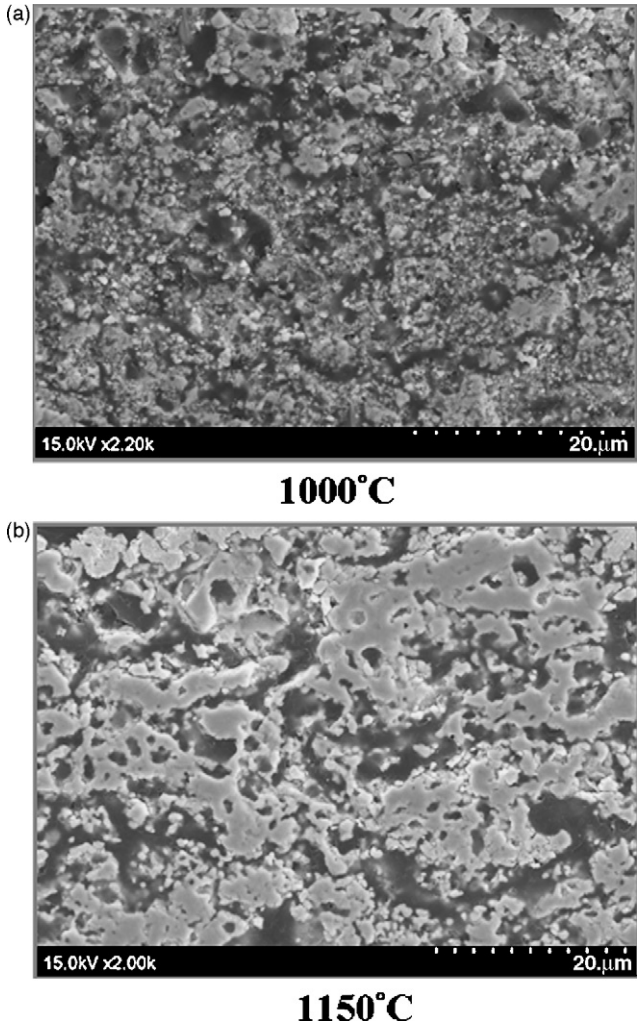

Fig. 25. Cathode cross-sectional microstructures of sprayed cells having heat treatments at (a) 1000 °C and (b) 1150 °C for 2 h, respectively.

4. Conclusions

Intermediate temperature solid oxide fuel cells with nanostructured YSZ/Ni anodes, LSGM electrolytes, LSCF cathodes and porous nickel metal supports have been fabricated successfully by atmospheric plasma spray technology with carefully selected spray parameters. As-sprayed cells were heated at different temperatures from 820 to 1150 °C for 2 h to remove carbon residue in LSCF cathodes, to search the optimized microstructure of LSCF cathodes and to increase particle bonding strengths between functional layers of cells. From analyzing measured ac impedance data at 800 °C by equivalent circuit fitting, variations of Re, Ra, Rc + Ws − r and Rp versus heat treatment temperature are obtained. It is found that anode resistance Ra is smaller than electrolyte resistance Re and cathode resistance contributed by Rc and Ws − r. For heat treatment temperatures less than 1100 °C, the variations of Re and Ra are small so that effects of structure variations of electrolyte and anode on cell performance are insignificant, but the variations of Rc + Ws − r and Rp are significant so that effect of cathode structure's variation on cell performance is significant. Because Rc + Ws − r and Rp have a minimum around 1000 °C, the APS sprayed cell after a heat treatment at 1000 °C for 2 h has a minimum inherent resistance with anode resistance Ra about 0.024 Ω cm^2, electrolyte resistance Re about 0.11 Ω cm^2 and total polarization resistance Rp about 0.11 Ω cm^2 at 800 °C and it can deliver maximum power densities of ∼440 mW cm^{-2} at 800 °C, ∼275 mW cm^{-2} at 750 °C and ∼170 mW cm^{-2} at 700 °C. The OCV value larger than 1 V indicates that the produced LSGM film has good gas tightness. The conductivity of this LSGM electrolyte with 60 μm in thickness is about 0.054 S cm^{-1}. The lower conductivity of APS sprayed LSGM film could be explained by the existence of closed pores inside the film. For heat treatment temperatures larger than 1100 °C, a significant element inter-diffusion between nanostructured YSZ/Ni anode and LSGM electrolyte occurs. This element inter-diffusion at high temperatures can

generate a high resistive material such as lanthanum–nickel oxide at anode–electrolyte interface so that electrolyte resistance Re and anode resistance Ra start to increase steeply. The steep increases of Rc + Ws − *r* and Rp indicate that the microstructure of LSCF cathode also changes to be unfavorable for oxygen mass transport and reduction. In this study, the best heat treatment temperature is around 1000 °C.

Acknowledgments

The authors are grateful to Prof. Chih-Hao Lee in Engineering and System Science Department of National Tsing Hua University for his valuable discussions.

References

[1] A.J. Appleby, Energy 21 (1996) 521–653.
[2] S.C. Singhal, MRS Bull. 25 (2000) 16–21.
[3] J.P.P. Hujismans, F.P.F. Van Berkel, G.M. Christie, J. Power Sources 71 (1998) 107–110.
[4] O. Yamamoto, Electochim. Acta 45 (2000) 2423–2435.
[5] F. Zhao, A. Virkar, J. Power Sources 141 (2005) 79–95.
[6] D. Lee, J.H. Han, Y. Chun, R.H. Song, D.R. Shin, J. Power Sources 166 (2007) 35–40.
[7] W. Gong, S. Gopalan, U.B. Pal, J. Power Sources 160 (2006) 305–315.
[8] K. Kuroda, I. Hashimoto, K. Adachi, J. Akikusa, Y. Tamou, N. Komada, T. Ishihara, Y. Takita, Solid State Ionics 132 (2000) 199–208.
[9] R. Zheng, X.M. Zhou, S.R. Wang, T.-L. Wen, C.X. Ding, J. Power Sources 140 (2005) 215–217.
[10] F. Tietz, V.A.C. Haanappel, A. Mai, J. Mertens, D. St¨over, J. Power Sources 156 (2006) 20–22.
[11] W.H. Kim, H.S. Song, J. Moon, H.W. Lee, Solid State Ionics 177 (2006) 3211–3216.
[12] A.V.Virkar, L. Wilson, Low Temperature Anode Supported High Power Density Solid Oxide Fuel Cells with Nanostructured Electrodes, Fuel Cell Annual Report, 2003.
[13] G. Meng, H. Song, Q. Dong, D. Peng, Soild State Ionics 175 (2004) 29–34.
[14] Y. Liu, M. Liu, J. Am. Ceram. Soc. 87 (2004) 2139–2142.
[15] J. Will, A. Mitterdorfer, C. Kleinlogel, D. Perednis, L.J. Gauckler, Solid State Ionics 131 (2000) 79–96.
[16] L.R. Pederson, P. Singh, X.-D. Zhou, Vacuum 80 (2006) 1066–1083.
[17] J.L. Young, T.H. Etsell, Solid State Ionics 135 (2000) 457–462.
[18] S. Zha, Y. Zhang, M. Liu, Solid State Ionics 176 (2005) 25–31.
[19] D. Simwonis, H. Thulen, F.J. Dias, A. Naoumidis, D. Stover, J. Mater. Process. Technol. 92–93 (1999) 107–115.
[20] J. Van herle, R. Ihringer, R. Vasquez Cavieres, L. Constantin, O. Bucheli, J. Eur. Ceram. Soc. 21 (2001) 1855–1859.
[21] C. Monterrubio-Badillo, H. Ageorges, T. Chartier, J.F. Coudert, P. Fauchais, Surf. Coat. Technol. 200 (2006) 3743–3756.
[22] J. Fazilleau, C. Delbos, V. Rat, J.F. Coudert, P. Fauchais, B. Pateyron, Plasma Chem. Plasma Proc. 26 (2006) 371–391.
[23] C. Hwang, C. Tzeng, J. Adv. Oxid. Technol. 8 (2005) 85–89.
[24] X. Zhang, S. Ohara, H. Okawa, R. Maric, T. Fukui, Solid State Ionics 139 (2001) 145–152.
[25] R. Hui, Z. Wang, O. Kesler, L. Rose, J. Jankovic, S. Yick, R. Maric, D. Ghosh, J. Power Sources 170 (2007) 308–323.
[26] R. Henne, J. Therm. Spray Technol. 16 (2007) 381–403.
[27] O. Kesler, Mater. Sci. Forum 539–543 (2007) 1385–1390.
[28] G. DiGiuseppe, Electrochem. Soc. Proc. 07 (2005) 322–333.
[29] X.Q. Ma, H. Zhang, J. Dai, J. Roth, R. Hui, T.D. Xiao, D.E. Reisner, J. Thermal Spray Technol. 14 (2005) 61–66.
[30] S. Hui, H. Zhang, X. Ma, J. Roth, T.D. Xiao, D.E. Reisner, Progress Report: Sequential-Fab Plasma-Sprayed components for Intermediate Temperature SOFCs Fuel Cell 2003—Proceedings of the Third Annual BCC Conference: Connections to Commercialism, Stamford, CT, USA, March 31—April 1, 2003.
[31] X. Ma, J. Dai, D. Reisner, Ceram. Ind. 154 (2004) 25–28.
[32] D. Stöver, D. Hathiramani, R. Vaßen, R.J. Daman, Surf. Coat. Technol. 201 (2006) 2002–2005.
[33] R. Vaßen, D. Hathiramani, J. Mertens, V.A.C. Haanappel, I.C. Vinke, Surf. Coat. Technol. 202 (2007) 499–508.
[34] X. Deng, A. Petric, J. Power Sources 140 (2005) 297–303.
[35] C. Hwang, C. Yu, Surf. Coat. Technol. 201 (2007) 5954–5959.
[36] C. Haavik, E.M. Ottesen, K. Nomura, J.A. Kilner, T. Norby, Solid State Ionics 174 (2004) 233–243.
[37] T. Ishihara, J.A. Kilner, M. Honda, N. Sakai, H. Yokokawa, Y. Takita, Solid State Ionics 113–115 (1998) 593–600.
[38] R.P. O'hayre, S.W. Cha, W. Colella, F.B. Prinz, Fuel Cell Fundamentals, John Wiley & Sons Inc., New York, 2006 (Chapter 7).
[39] Y. Qi, B. Huang, K.T. Chuang, J. Power Sources 150 (2005) 32–47.
[40] S.P. Jiang, J.G. Love, Y. Ramprakash, J. Power Sources 110 (2002) 201–208.
[41] E. Lust, P. Möller, I. Kivi, G. Nurk, S. Kallip, P. Nigu, K. Lust, J. Electrochem. Soc. 152 (2005) A2306–A2308.